

RECEIVED: January 14, 2015

REVISED: March 3, 2015

ACCEPTED: March 11, 2015

PUBLISHED: April 14, 2015

Angular analysis of the $B^0 \rightarrow K^{*0} e^+ e^-$ decay in the low- q^2 region



The LHCb collaboration

E-mail: schunem@lal.in2p3.fr

ABSTRACT: An angular analysis of the $B^0 \rightarrow K^{*0} e^+ e^-$ decay is performed using a data sample, corresponding to an integrated luminosity of 3.0 fb^{-1} , collected by the LHCb experiment in pp collisions at centre-of-mass energies of 7 and 8 TeV during 2011 and 2012. For the first time several observables are measured in the dielectron mass squared (q^2) interval between 0.002 and $1.120 \text{ GeV}^2/c^4$. The angular observables F_L and A_T^{Re} which are related to the K^{*0} polarisation and to the lepton forward-backward asymmetry, are measured to be $F_L = 0.16 \pm 0.06 \pm 0.03$ and $A_T^{\text{Re}} = 0.10 \pm 0.18 \pm 0.05$, where the first uncertainty is statistical and the second systematic. The angular observables $A_T^{(2)}$ and A_T^{Im} which are sensitive to the photon polarisation in this q^2 range, are found to be $A_T^{(2)} = -0.23 \pm 0.23 \pm 0.05$ and $A_T^{\text{Im}} = 0.14 \pm 0.22 \pm 0.05$. The results are consistent with Standard Model predictions.

KEYWORDS: Rare decay, Polarization, B physics, Flavour Changing Neutral Currents, Hadron-Hadron Scattering

ARXIV EPRINT: [1501.03038](https://arxiv.org/abs/1501.03038)

Contents

1	Introduction	1
2	The LHCb detector and data set	4
3	Selection of signal candidates	5
4	Exclusive and partially reconstructed backgrounds	7
5	Fit to the $K^+\pi^-e^+e^-$ invariant mass distribution	8
6	Angular acceptance and angular modelling of the backgrounds	9
6.1	Angular acceptance	9
6.2	Angular modelling of the backgrounds	10
7	Measurement of the angular observables	11
7.1	Fit results	11
7.2	Systematic uncertainties	11
7.3	Effective q^2 range of the selected $B^0 \rightarrow K^{*0}e^+e^-$ signal events	13
8	Summary	14
	The LHCb collaboration	18

1 Introduction

The $B^0 \rightarrow K^{*0}e^+e^-$ decay is a flavour changing neutral current process that is mediated by electroweak box and loop diagrams in the Standard Model (SM). Charge conjugation is implied throughout this paper unless stated otherwise and the K^{*0} represents the $K^{*0}(892)$, reconstructed as $K^{*0} \rightarrow K^+\pi^-$. The angular distribution of the $K^+\pi^-e^+e^-$ system is particularly sensitive to contributions from non-SM physics (NP). The leading SM diagrams are shown in figure 1; the relative contribution of each of the diagrams varies with the dilepton invariant mass. In the region where the dilepton invariant mass squared (q^2) is less than $6 \text{ GeV}^2/c^4$, some theoretical uncertainties from long distance contributions are greatly reduced, thereby allowing more control over the SM prediction and increasing sensitivity to any NP effect [1, 2]. Furthermore, the contribution from a virtual photon coupling to the lepton pair dominates in the very low q^2 region, allowing measurement of the helicity of the photon in $b \rightarrow s\gamma$ transitions [3, 4]. In the SM, this photon is predominantly left-handed, with a small right-handed component arising from the mass of the s quark and long distance effects. In contrast, in many extension of the SM, NP may manifest as a large right handed current, see for example refs. [5–8].

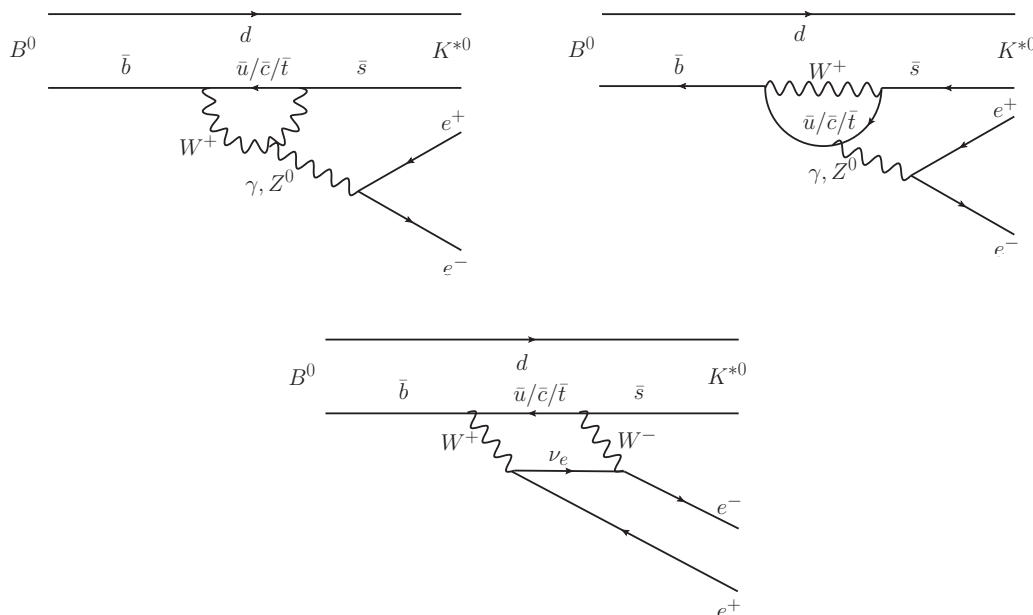


Figure 1: Dominant Standard Model Feynman graphs for the electroweak loop and box diagrams involved in the $B^0 \rightarrow K^{*0} e^+ e^-$ decay.

The q^2 region below $1 \text{ GeV}^2/c^4$ has previously been studied through the analysis of the $B^0 \rightarrow K^{*0} \ell^+ \ell^-$ ($\ell = e, \mu$) [9–11]. Experimentally, an analysis with muons rather than electrons in the final state produces a much higher yield at LHCb. This is primarily due to the distinctive signature that muons provide, which is efficiently exploited in the online selection, together with the better mass and energy resolutions and higher reconstruction efficiency of dimuon decays. However, as outlined in ref. [12], dielectron decays at low q^2 provide greater sensitivity to the photon polarisation and therefore to the C_7 and C'_7 Wilson coefficients, which are associated with the left-handed and right-handed electromagnetic operators, respectively [3]. Due to the muon mass, the virtual photon contribution in dimuon decays is suppressed relative to dielectron decays. Additionally, the formalism for the $B^0 \rightarrow K^{*0} e^+ e^-$ decay is greatly simplified as the electron mass can be neglected. Indeed, the decay with electrons allows for an angular analysis down to a q^2 of $0.0004 \text{ GeV}^2/c^4$. However, above a q^2 of $1 \text{ GeV}^2/c^4$, the muon mass terms become negligible and the electron and muon modes have essentially the same functional dependence on the Wilson coefficients (within the lepton flavour universality assumption).

This work is based on a previous analysis performed by the LHCb collaboration to measure the $B^0 \rightarrow K^{*0} e^+ e^-$ branching fraction with an integrated luminosity of 1.0 fb^{-1} [13], with the selection re-optimised for the angular analysis.

The partial decay width of the $B^0 \rightarrow K^{*0} e^+ e^-$ decay can be described in terms of q^2 and three angles, θ_ℓ, θ_K and ϕ . The angle θ_ℓ is defined as the angle between the direction of the e^+ (e^-) and the direction opposite to that of the B^0 (\bar{B}^0) meson in the dielectron rest frame. The angle θ_K is defined as the angle between the direction of the kaon and

the direction opposite to that of the B^0 (\bar{B}^0) meson in the K^{*0} (\bar{K}^{*0}) rest frame. The angle ϕ is the angle between the plane containing the e^+ and e^- and the plane containing the kaon and pion from the K^{*0} (\bar{K}^{*0}) in the B^0 (\bar{B}^0) rest frame. The basis is designed such that the angular definition for the \bar{B}^0 decay is a CP transformation of that for the B^0 decay. These definitions are identical to those used for the $B^0 \rightarrow K^{*0} \mu^+ \mu^-$ analysis [10]. As in ref. [10], the angle ϕ is transformed such that $\tilde{\phi} = \phi + \pi$ if $\phi < 0$, to compensate for the limited signal yield. This transformation cancels out the terms that have a $\sin \phi$ or $\cos \phi$ dependence and simplifies the angular expression without any loss of sensitivity to the remaining observables. In the limit of massless leptons and neglecting the $K^+ \pi^-$ S-wave contribution, which is expected to be negligible¹ at low q^2 with the current sample size [14], the $B^0 \rightarrow K^{*0} e^+ e^-$ angular distribution reads as

$$\frac{1}{d(\Gamma + \bar{\Gamma})/dq^2} \frac{d^4(\Gamma + \bar{\Gamma})}{dq^2 d\cos\theta_\ell d\cos\theta_K d\tilde{\phi}} = \frac{9}{16\pi} \left[\frac{3}{4}(1 - F_L) \sin^2\theta_K + F_L \cos^2\theta_K + \left(\frac{1}{4}(1 - F_L) \sin^2\theta_K - F_L \cos^2\theta_K\right) \cos 2\theta_\ell + \frac{1}{2}(1 - F_L) A_T^{(2)} \sin^2\theta_K \sin^2\theta_\ell \cos 2\tilde{\phi} + (1 - F_L) A_T^{\text{Re}} \sin^2\theta_K \cos\theta_\ell + \frac{1}{2}(1 - F_L) A_T^{\text{Im}} \sin^2\theta_K \sin^2\theta_\ell \sin 2\tilde{\phi} \right]. \quad (1.1)$$

The four angular observables F_L , $A_T^{(2)}$, A_T^{Re} and A_T^{Im} are related to the transversity amplitudes through [2]

$$\begin{aligned} F_L &= \frac{|A_0|^2}{|A_0|^2 + |A_{||}|^2 + |A_{\perp}|^2} \\ A_T^{(2)} &= \frac{|A_{\perp}|^2 - |A_{||}|^2}{|A_{\perp}|^2 + |A_{||}|^2} \\ A_T^{\text{Re}} &= \frac{2\mathcal{R}e(A_{||L} A_{\perp L}^* + A_{||R} A_{\perp R}^*)}{|A_{||}|^2 + |A_{\perp}|^2} \\ A_T^{\text{Im}} &= \frac{2\mathcal{I}m(A_{||L} A_{\perp L}^* + A_{||R} A_{\perp R}^*)}{|A_{||}|^2 + |A_{\perp}|^2}, \end{aligned} \quad (1.2)$$

where $|A_0|^2 = |A_{0L}|^2 + |A_{0R}|^2$, $|A_{\perp}|^2 = |A_{\perp L}|^2 + |A_{\perp R}|^2$ and $|A_{||}|^2 = |A_{||L}|^2 + |A_{||R}|^2$. The amplitudes A_0 , $A_{||}$ and A_{\perp} correspond to different polarisation states of the K^{*0} in the decay. The labels L and R refer to the left and right chirality of the dielectron system.

Given the definition of $\tilde{\phi}$, the observable $A_T^{(2)}$ is averaged between B^0 and \bar{B}^0 decays, while A_T^{Im} corresponds to a CP asymmetry [15]. The observable F_L is the longitudinal polarisation of the K^{*0} and is expected to be small at low q^2 , since the virtual photon

¹Using refs. [1, 14] it can be shown that the ratio of the S-wave fraction to the fraction of longitudinal polarisation of the K^{*0} is constant as function of q^2 in the 0-6 GeV²/c⁴ range.

is then quasi-real and therefore transversely polarised. The observable A_{T}^{Re} is related to the forward-backward asymmetry A_{FB} by $A_{\text{T}}^{\text{Re}} = \frac{4}{3}A_{\text{FB}}/(1 - F_{\text{L}})$ [2]. The observables $A_{\text{T}}^{(2)}$ and A_{T}^{Im} , in the limit $q^2 \rightarrow 0$, can be expressed as simple functions of the \mathcal{C}_7 and \mathcal{C}'_7 coefficients [2]

$$A_{\text{T}}^{(2)}(q^2 \rightarrow 0) = \frac{2\mathcal{R}e(\mathcal{C}_7\mathcal{C}'_7^*)}{|\mathcal{C}_7|^2 + |\mathcal{C}'_7|^2} \quad \text{and} \quad A_{\text{T}}^{\text{Im}}(q^2 \rightarrow 0) = \frac{2\mathcal{I}m(\mathcal{C}_7\mathcal{C}'_7^*)}{|\mathcal{C}_7|^2 + |\mathcal{C}'_7|^2}. \quad (1.3)$$

These measurements therefore provide information on photon polarisation amplitudes, similar to that obtained by the CP asymmetry measured through time-dependent analyses in $B^0 \rightarrow K^{*0}(\rightarrow K_{\text{S}}^0\pi^0)\gamma$ decays [16, 17].

This paper presents measurements of F_{L} , $A_{\text{T}}^{(2)}$, A_{T}^{Im} and A_{T}^{Re} of the $B^0 \rightarrow K^{*0}e^+e^-$ decay in the bin corresponding to a reconstructed q^2 from 0.0004 to 1 GeV²/c⁴.

2 The LHCb detector and data set

The study reported here is based on pp collision data, corresponding to an integrated luminosity of 3.0 fb⁻¹, collected at the Large Hadron Collider (LHC) with the LHCb detector [18, 19] at centre-of-mass energies of 7 and 8 TeV during 2011 and 2012. The LHCb detector is a single-arm forward spectrometer covering the pseudorapidity range $2 < \eta < 5$, designed for the study of particles containing b or c quarks. The detector includes a high-precision tracking system consisting of a silicon-strip vertex detector surrounding the pp interaction region [20], a large-area silicon-strip detector located upstream of a dipole magnet with a bending power of about 4 Tm, and three stations of silicon-strip detectors and straw drift tubes [21] placed downstream of the magnet. The tracking system provides a measurement of momentum, p , with a relative uncertainty that varies from 0.5% at low momentum to 1.0% at 200 GeV/c. The minimum distance of a track to a primary vertex, the impact parameter (IP), is measured with a resolution of $(15 + 29/p_{\text{T}})\mu\text{m}$, where p_{T} is the component of the momentum transverse to the beam, in GeV/c. Different types of charged hadrons are distinguished using information from two ring-imaging Cherenkov detectors [22]. Photons, electrons and hadrons are identified by a calorimeter system consisting of scintillating-pad and preshower detectors, an electromagnetic calorimeter (ECAL) and a hadronic calorimeter. Muons are identified by a system composed of alternating layers of iron and multiwire proportional chambers [23].

The trigger [24] consists of a hardware stage, based on information from the calorimeter and muon systems, followed by a software stage, which applies a full event reconstruction. For signal candidates to be considered in this analysis, all tracks from the $B^0 \rightarrow K^{*0}e^+e^-$ decay must have hits in the vertex detector and at least one of the tracks from the $B^0 \rightarrow K^{*0}e^+e^-$ decay must meet the requirements of the hardware electron or hadron triggers, or the hardware trigger must be fulfilled independently of any of the decay products of the signal B^0 candidate (usually triggering on the other b hadron in the event). The hardware electron trigger requires the presence of an ECAL cluster with a minimum transverse energy between 2.5 GeV and 2.96 GeV depending on the data taking period. The hardware hadron trigger requires the presence of a cluster in the hadron calorimeter with a transverse energy greater

than 3.5 GeV. The software trigger requires a two-, three- or four-track secondary vertex with a significant displacement from the primary pp interaction vertices (PVs). At least one charged particle must have a transverse momentum $p_T > 1.7 \text{ GeV}/c$ and be inconsistent with originating from the PV. A multivariate algorithm [25] is used for the identification of secondary vertices consistent with the decay of a b hadron.

Samples of simulated $B^0 \rightarrow K^{*0}e^+e^-$ events are used to determine the efficiency to trigger, reconstruct and select signal events. In addition, specific samples of simulated events are utilised to estimate the contribution from exclusive backgrounds and to model their mass and angular distributions. The pp collisions are generated using PYTHIA [26] with a specific LHCb configuration [28]. Decays of hadronic particles are described by EVTGEN [29], in which final-state radiation is generated using PHOTOS [30]. The interaction of the generated particles with the detector, and its response, are implemented using the GEANT4 toolkit [31] as described in ref. [33]. The simulated samples are corrected for known differences between data and simulation in particle identification [22], detector occupancy and hardware trigger efficiency.

3 Selection of signal candidates

Bremsstrahlung radiation, if not accounted for, would worsen the B^0 mass resolution. If the radiation occurs downstream of the dipole magnet, the momentum of the electron is correctly measured and the photon energy is deposited in the same calorimeter cell as the electron. If photons are emitted upstream of the magnet, the electron momentum is evaluated after photon emission, and the measured B^0 mass is shifted. In general, these bremsstrahlung photons deposit their energy in different calorimeter cells than those hit by the electron. In both cases, the ratio of the energy detected in the ECAL to the momentum measured by the tracking system, an important variable in identifying electrons, remains unbiased. To improve the momentum reconstruction, a dedicated bremsstrahlung recovery is used. Contributions from photon candidates, neutral clusters with transverse energy greater than 75 MeV, found within a region of the ECAL defined by the extrapolation of the electron track upstream of the magnet, are added to the measured electron momentum.

Oppositely charged electron pairs formed from tracks with p_T exceeding 350 MeV/ c and with a good-quality vertex are used to form signal candidates. If the same bremsstrahlung photon is associated with both the e^+ and the e^- , its energy is added randomly to one of the tracks. The reconstructed e^+e^- invariant mass is required to be in the range 20–1000 MeV/ c^2 ($0.0004 < q^2 < 1 \text{ GeV}^2/c^4$). The choice of the lower bound is a compromise between the gain in sensitivity to the photon polarisation from measuring as low as possible in q^2 and a degradation of the resolution in $\tilde{\phi}$ as q^2 decreases, due to multiple scattering, as shown in figure 2. The lower bound requirement at 20 MeV/ c^2 on the e^+e^- invariant mass also serves to reduce the background from $B^0 \rightarrow K^{*0}\gamma$ decays followed by a photon conversion in the material, noted below as $B^0 \rightarrow K^{*0}\gamma_{e^+e^-}$.

Candidate K^{*0} mesons are reconstructed in the $K^{*0} \rightarrow K^+\pi^-$ mode where the p_T of the K^+ (π^-) meson is required to be larger than 400 (300) MeV/ c and charged pions and kaons are identified using information from the RICH detectors.

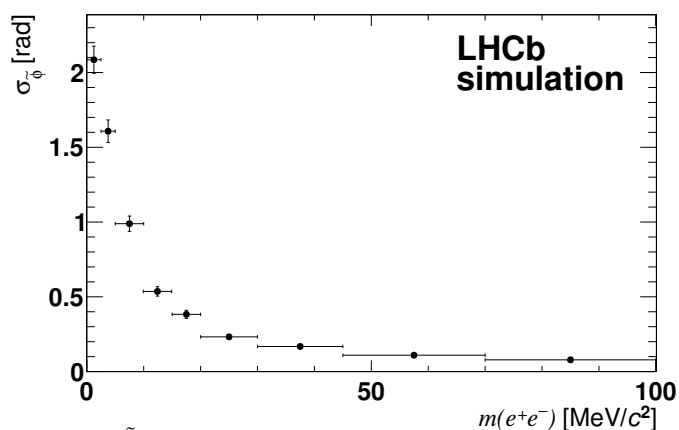


Figure 2: Resolution on the $\tilde{\phi}$ angle as a function of the e^+e^- invariant mass as obtained from LHCb simulated events.

Candidate K^{*0} mesons and e^+e^- pairs are required to have a common good-quality vertex to form B^0 candidates. When more than one PV is reconstructed, the one giving the smallest IP χ^2 for the B^0 candidate is chosen. The reconstructed decay vertex of the B^0 candidate is required to be significantly separated from the PV and the candidate momentum direction to be consistent with its direction of flight from the PV. The B^0 mass resolution, the angular acceptance and the rates of physics and combinatorial backgrounds depend on how the event was triggered. The data sample is therefore divided into three mutually exclusive categories: events for which one of the electrons from the B^0 decay satisfies the hardware electron trigger, events for which one of the hadrons from the B^0 decay satisfies the hardware hadron trigger and events triggered by activity in the event not due to any of the signal decay particles.

In order to maximise the signal efficiency while reducing the high level of combinatorial background, a multivariate classifier based on a boosted decision tree algorithm (BDT) [34, 35] is used. The signal training sample is composed of simulated $B^0 \rightarrow K^{*0}e^+e^-$ events and the background training sample is taken from the upper invariant mass sideband ($m(K^+\pi^-e^+e^-) > 5600 \text{ MeV}/c^2$) of $B^0 \rightarrow K^{*0}e^+e^-$ decays reconstructed in half of the data sample. Two separate BDTs are used, one each for half of the data sample. They are optimised separately and applied to the complementary half of the data in order to avoid any potential bias due to the use of the data upper sideband for the background sample. The BDT uses information about the event kinematic properties, vertex and track quality, IP and p_T of the tracks, flight distance from the PV as well as information about isolation of the final state particles.² The selection is optimised to maximise $N_S/\sqrt{N_S + N_B}$ separately for the three trigger categories and the two BDTs through a grid search of the set of criteria for the particle identification of the four final state particles and the BDT response. The background yield (N_B) is extrapolated into the signal range using the $m(K^+\pi^-e^+e^-)$ distribution outside a $\pm 300 \text{ MeV}/c^2$ window around the known B^0 mass. The expected signal

²The isolation is defined as the number of good two-track vertices that one of the candidate signal tracks can make with any other track in the event [36].

yield (N_S) is obtained using the $B^0 \rightarrow K^{*0}e^+e^-$ simulation and the known $B^0 \rightarrow K^{*0}e^+e^-$ branching fraction [13], and correcting for data-to-simulation differences in the selection efficiency obtained using the well known $B^0 \rightarrow J/\psi(e^+e^-)K^{*0}$ decay. The efficiency of this requirement on the selected signal is 93% while the background is reduced by two orders of magnitude. The expected values for $N_S/\sqrt{N_S+N_B}$ range from 3.9 to 7.5 depending on the trigger category.

4 Exclusive and partially reconstructed backgrounds

Several sources of background are studied using samples of simulated events, corrected to reflect the difference in particle identification performances between data and simulation.

A large non-peaking background comes from the $B^0 \rightarrow D^-e^+\nu$ decay, with $D^- \rightarrow e^-\bar{\nu}K^{*0}$ which has a combined branching fraction about four orders of magnitude larger than that of the signal. In the rare case where both neutrinos have low energies, the signal selection is ineffective at rejecting this background which tends to peak towards $\cos\theta_\ell \approx 1$. In order to avoid any potential bias in the measurement of the A_T^{Re} parameter, a symmetric requirement of $|\cos\theta_\ell| < 0.8$ is applied to suppress this background, resulting in a loss of signal of the order of 10%.

To suppress background from $B_s^0 \rightarrow \phi e^+e^-$ decays, with $\phi \rightarrow K^+K^-$, where one of the kaons is misidentified as a pion, the two-hadron invariant mass computed under the K^+K^- hypothesis is required to be larger than $1040 \text{ MeV}/c^2$.

Background from the decay $\Lambda_b^0 \rightarrow pK^-e^+e^-$ is suppressed by rejecting events where the pion is consistent with being a proton, according to the information from the RICH detectors.

The probability for a decay $B^0 \rightarrow K^{*0}e^+e^-$ to be misidentified as $\bar{B}^0 \rightarrow \bar{K}^{*0}e^+e^-$ is estimated to be 1.1 % using simulated events and this background is therefore neglected.

Another important source of background comes from the $B^0 \rightarrow K^{*0}\gamma$ decay, where the photon converts into an e^+e^- pair. In LHCb, approximately 40% of the photons convert before reaching the calorimeter, and although only about 10% are reconstructed as an e^+e^- pair with hits in the vertex detector, the resulting mass of the B^0 candidate peaks in the signal region. Two very effective criteria for suppressing this background are the minimum requirement on the e^+e^- invariant mass, $m(e^+e^-) > 20 \text{ MeV}/c^2$, and a requirement that the uncertainty of the reconstructed z coordinate of the e^+e^- pair, $\sigma_z(e^+e^-)$, is less than 30 mm. These requirements reject more than 99% of simulated $B^0 \rightarrow K^{*0}\gamma$ events. The remaining contamination is estimated by normalising the simulated $B^0 \rightarrow K^{*0}\gamma_{e^+e^-}$ to the observed yield without the $\sigma_z(e^+e^-)$ criterion and requiring the e^+e^- invariant mass to be lower than $5 \text{ MeV}/c^2$. The residual contamination from $B^0 \rightarrow K^{*0}\gamma$ decays is $(3.8 \pm 1.9)\%$ of the signal yield. Part of this background comes from low-mass e^+e^- pairs that are reconstructed at larger masses due to multiple scattering. The remainder comes from direct Bethe-Heitler pair-production at masses larger than $20 \text{ MeV}/c^2$. To obtain an accurate estimate of this component, the GEANT4 simulation is reweighted as a function of the true e^+e^- mass to match the distribution of ref. [37] since GEANT4 does not model correctly the high-mass e^+e^- pair production.

Another possible source of contamination is the decay $B^0 \rightarrow K^{*0}V(\rightarrow e^+e^-)$ where V is a ρ , ω or ϕ meson. Expected rates for these backgrounds have been evaluated in refs. [4, 38]. The effects of direct decays or interference with the signal decay are found to be negligible after integrating over the q^2 range.

Partially reconstructed (PR) backgrounds arising from $B^0 \rightarrow K^{*0}e^+e^-X$ decays, where one or more of the decay products (X) from the B^0 decay is not reconstructed, are also taken into account. These incomplete events are mostly due to decays involving higher K^* resonances, hereafter referred to as K^{**} . The decays $B^0 \rightarrow K^{*0}\eta$ and $B^0 \rightarrow K^{*0}\pi^0$ are also studied and several cases are considered: the case when the e^+e^- pair comes from a converted photon in the material, the case when the e^+ and e^- originate from the conversions of the two photons and finally the case of the Dalitz decay of the η or the π^0 . They contribute about 25% of the PR background in the angular fitting domain.

5 Fit to the $K^+\pi^-e^+e^-$ invariant mass distribution

In a first step, a mass fit over a wide mass range, from 4300 to 6300 MeV/ c^2 , is performed to estimate the size of the $B^0 \rightarrow K^{*0}e^+e^-$ signal, the combinatorial background and the PR background. The fractions of each component are determined from unbinned maximum likelihood fits to the mass distributions separately for each trigger category. The mass distribution of each category is fitted to a sum of probability density functions (PDFs), modelling the different components. Following the strategy of ref. [39], the signal PDF depends on the number of neutral clusters that are added to the dielectron candidate to correct for the effects of bremsstrahlung. The signal is described by the sum of a Crystal Ball function [40] (CB) and a wide Gaussian function accounting for the cases where background photons have been associated; the CB function accounts for over 90% of the total signal PDF. The shape of the combinatorial background is parameterised by an exponential function. Finally, the shape of the PR background is described by non-parametric PDFs [41] determined from fully simulated events passing the selection.

The signal shape parameters are fixed to the values obtained from fits to simulation but the widths and mean values are corrected for data simulation differences using $B^0 \rightarrow J/\psi(e^+e^-)K^{*0}$ as a control channel. Since the photon pole contribution dominates in the low- q^2 region, the PR background is expected to be similar for $B^0 \rightarrow K^{*0}e^+e^-$ and $B^0 \rightarrow K^{*0}\gamma$. The large branching fraction of the decay $B^0 \rightarrow K^{*0}\gamma$ allows the fractions of PR background relative to the signal yield to be determined from the data. These fractions are extracted from a fit to a larger sample of events obtained by removing the requirements on the lower bound of the e^+e^- invariant mass and on $\sigma_z(e^+e^-)$ and therefore dominated by $B^0 \rightarrow K^{*0}\gamma_{e^+e^-}$ events. The invariant mass distribution, together with the PDFs resulting from this fit, is shown in figure 3(a) for the three trigger categories grouped together. The corresponding distribution for the $B^0 \rightarrow K^{*0}e^+e^-$ fit is shown in figure 3(b). There are 150 ± 17 $B^0 \rightarrow K^{*0}e^+e^-$ signal events, 106 ± 16 PR background events and 681 ± 32 combinatorial background events in the 4300–6300 MeV/ c^2 window.

In this wide mass window, the sample is dominated by combinatorial background, whose angular shape is difficult to model. Furthermore the angular distributions depend

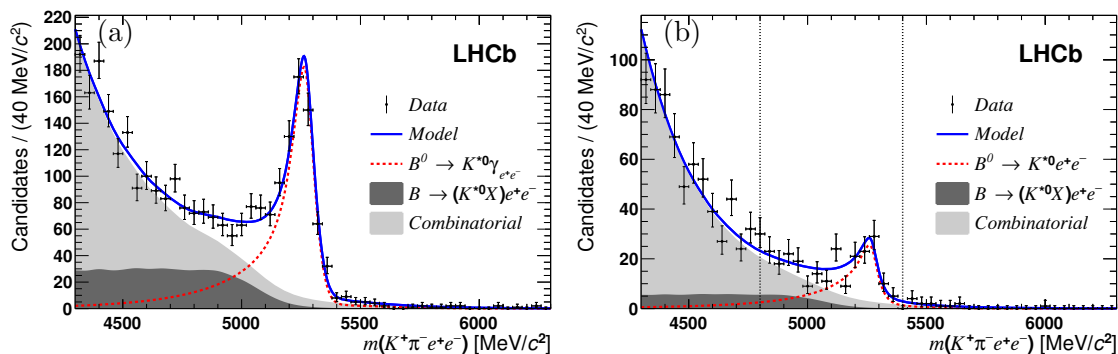


Figure 3: Invariant mass distribution for (a) the $B^0 \rightarrow K^{*0} \gamma e^+ e^-$ and (b) the $B^0 \rightarrow K^{*0} e^+ e^-$ decay modes and the three trigger categories grouped together. The dashed line is the signal PDF, the light grey area corresponds to the combinatorial background and the dark grey area is the PR background. The solid line is the total PDF. The two vertical dotted lines on the $B^0 \rightarrow K^{*0} e^+ e^-$ plot indicate the signal window that is used in the angular fit.

on the kinematic properties of the background and may thus vary as functions of mass. Hence, the angular fit is performed in a narrower mass window from $4800 \text{ MeV}/c^2$ to $5400 \text{ MeV}/c^2$. In this restricted window there are 124 $B^0 \rightarrow K^{*0} e^+ e^-$ signal events, 38 PR and 83 combinatorial background events, corresponding to a signal-to-background ratio of the order of one. About half of these events belong to the electron hardware trigger category and the rest are equally distributed between the other two categories.

6 Angular acceptance and angular modelling of the backgrounds

6.1 Angular acceptance

The angular acceptance is factorised as $\varepsilon(\cos \theta_\ell, \cos \theta_K, \tilde{\phi}) = \varepsilon(\cos \theta_\ell) \varepsilon(\cos \theta_K) \varepsilon(\tilde{\phi})$ as supported by simulation studies. The three corresponding one-dimensional angular distributions for the $B^0 \rightarrow K^{*0} e^+ e^-$ decay are distorted by the geometrical acceptance of the detector, the trigger, the event reconstruction and the selection. Furthermore, their precise shapes depend upon the various trigger categories, each being enriched in events with different kinematic properties. For the $\tilde{\phi}$ angle, a uniform acceptance is expected. However, there are distortions in both the $\cos \theta_\ell$ and $\cos \theta_K$ distributions, mainly arising from requirements on the transverse momenta of the particles. The $\cos \theta_K$ acceptance is asymmetric due to the momentum imbalance between the kaon and the pion from the K^{*0} decay in the laboratory frame due to their different masses. The $\cos \theta_K$ and $\cos \theta_\ell$ acceptance distributions are modelled on simulated $B^0 \rightarrow K^{*0} e^+ e^-$ events with Legendre polynomials of fourth order. The functions chosen to model the $\cos \theta_\ell$ acceptance are assumed to be symmetric and modified by a linear term to estimate the systematic uncertainty on the A_T^{Re} parameter. For the $\tilde{\phi}$ acceptance, no significant deviation from uniformity is observed. To estimate the systematic uncertainty, modulations in $\cos 2\tilde{\phi}$ or $\sin 2\tilde{\phi}$ are allowed. Such modulations are the most harmful ones since they may be confused with physics processes yielding non-zero values of $A_T^{(2)}$ or A_T^{Im} .

6.2 Angular modelling of the backgrounds

In the mass window $4800 < m(K^+\pi^-e^+e^-) < 5400 \text{ MeV}/c^2$ used in the angular analysis, about one third of the events are combinatorial background. The angular distribution of these events is described by the product of three independent distributions for $\cos\theta_\ell$, $\cos\theta_K$ and $\tilde{\phi}$. This background largely dominates at low $m(K^+\pi^-e^+e^-)$: between $4300 \text{ MeV}/c^2$ and $4800 \text{ MeV}/c^2$, about 90% of the events are combinatorial background according to the mass fit shown in figure 3. However, the angular distributions of the background depend upon $m(K^+\pi^-e^+e^-)$ and the information from the lower mass window cannot be used directly for modelling the signal region. The effect of this correlation is extracted from a sample of data events selected with a looser BDT requirement but excluding the region of the BDT response corresponding to the signal. With this selection the sample is dominated by background in the whole mass range. The $\cos\theta_K$ background distributions are modelled as first order polynomials. The $\cos\theta_\ell$ background distributions are modelled with polynomial functions with third and fourth order terms. The $\tilde{\phi}$ distributions are compatible with being uniform. This method assumes that there is no strong correlation between the BDT response and $m(K^+\pi^-e^+e^-)$. This assumption is tested by subdividing the sample of events with looser BDT response and comparing the differences between the angular shapes predicted by this procedure and those observed. These differences are smaller than the statistical uncertainties of the parameters used to describe the angular shapes. The statistical uncertainties are thus used to assess the size of the systematic uncertainties due to the combinatorial background modelling.

The PR background accounts for about 15% of the events in the angular fit mass window. These events cannot be treated in the same way as the combinatorial ones. Since only one or two particles are not reconstructed, the observed angular distributions retain some of the features induced by the dynamics of the decay. Hence, they are modelled using the same functional shapes as the signal, but with independent physics parameters, $F_{L,PR}$, $A_{T,PR}^{(2)}$, $A_{T,PR}^{Im}$ and $A_{T,PR}^{Re}$. The loss of one or more final-state hadrons leads to a smaller apparent polarisation of the K^{*0} . While on $B^0 \rightarrow K^{*0}\gamma$ simulated events the F_L parameter is found to be zero, it reaches 17% for simulated $B \rightarrow \gamma K^{**}(\rightarrow K\pi X)$ events. Since in the SM one expects an F_L value of the order of 15 to 20%, $F_{L,PR}$ is assumed to be equal to $1/3$, which is equivalent to no polarisation. This parameter is varied between 17% and 50% to assess the size of the systematic uncertainty associated with this hypothesis. Similarly, the loss of information due to the unreconstructed particles leads to a damping of the transverse asymmetries of the PR background, $A_{T,PR}^{(2)}$, $A_{T,PR}^{Im}$ and $A_{T,PR}^{Re}$, compared to those of the signal. The signal transverse asymmetries are expected to be small in the SM, therefore their values are set to zero to describe the angular shape of the PR background. For $A_{T,PR}^{(2)}$ and $A_{T,PR}^{Im}$ the validity of this assumption is tested by comparing angular fits to $B \rightarrow J/\psi K^{**}(\rightarrow K\pi X)$ and $B^0 \rightarrow J/\psi K^{*0}$ simulated events, which confirms a damping factor compatible with zero. The systematic uncertainty associated with this assumption is estimated by varying $A_{T,PR}^{(2)}$ and $A_{T,PR}^{Im}$ up to half of the fitted signal values of $A_T^{(2)}$ and A_T^{Im} , *i.e.* assuming a damping factor of 0.5. For the $A_{T,PR}^{Re}$ parameter, however, one cannot estimate a damping factor with the same method since in the $B \rightarrow J/\psi K^{*0}$ decay the value

of A_T^{Re} is zero. The systematic uncertainty is evaluated by allowing the $A_{T,\text{PR}}^{\text{Re}}$ parameter to be as high as the A_T^{Re} value obtained from the $B^0 \rightarrow K^{*0} e^+ e^-$ angular fit.

7 Measurement of the angular observables

7.1 Fit results

To measure the four angular observables, F_L , $A_T^{(2)}$, A_T^{Im} and A_T^{Re} , an unbinned maximum likelihood fit is performed on the $m(K^+ \pi^- e^+ e^-)$, $\cos \theta_\ell$, $\cos \theta_K$ and $\tilde{\phi}$ distributions in the signal window defined in section 5. The inclusion of $m(K^+ \pi^- e^+ e^-)$ in the fit strongly improves its statistical power since the level of background varies significantly within the signal mass window. The fit is performed simultaneously on the three trigger categories sharing the fit parameters associated with the angular observables. The mass PDFs for the three components (signal, PR background and combinatorial background) are obtained from the fit described in section 5. The angular PDFs for the signal are obtained by multiplying the formula of eq. 1.1 by the acceptance described in section 6. Similarly, the angular PDFs for the PR background are modelled by using eq. 1.1 and the acceptance described in section 6 and setting $F_{L,\text{PR}} = 0.33$ and $A_{T,\text{PR}}^{(2)} = A_{T,\text{PR}}^{\text{Im}} = A_{T,\text{PR}}^{\text{Re}} = 0$. Finally, the angular PDFs for the combinatorial background are described in section 6. The combinatorial and PR background fractions are constrained to the values calculated from the mass fit described in section 5. The fit is validated using a large number of pseudo-experiments that include all the components of the fits. Several input values for the angular observables, F_L , $A_T^{(2)}$, A_T^{Im} and A_T^{Re} , are studied including those associated with NP models, and the fit results are in good agreement with the inputs. The fitting procedure is also verified using a large sample of fully simulated events; the fitted values of F_L , $A_T^{(2)}$, A_T^{Im} and A_T^{Re} are in excellent agreement with the generated ones. This validates not only the fit but also the assumption that the angular acceptance factorises. The distributions of $m(K^+ \pi^- e^+ e^-)$, $\cos \theta_\ell$, $\cos \theta_K$ and $\tilde{\phi}$, together with the likelihood projections resulting from the fit, are shown in figure 4 and the fit results are given in table 1. The fitted values of F_L , $A_T^{(2)}$, A_T^{Im} and A_T^{Re} are corrected for the $(3.8 \pm 1.9)\%$ contamination from $B^0 \rightarrow K^{*0} \gamma e^+ e^-$ decays, assuming that $F_{L,K^{*0}\gamma}$, $A_{T,K^{*0}\gamma}^{(2)}$, $A_{T,K^{*0}\gamma}^{\text{Im}}$ and $A_{T,K^{*0}\gamma}^{\text{Re}}$ are all equal to zero, and are used for the computation of the systematic uncertainties related to the angular description of the PR background. The fitted values are also corrected for the small fit biases due to the limited size of the data sample.

7.2 Systematic uncertainties

To evaluate the contributions from the possible sources of systematic uncertainty, pseudo-experiments with modified parameters are generated and fitted with the PDFs used to fit the data. Fit results are then compared with input values to assess the size of the uncertainties.

The systematic uncertainties due to the modelling of the angular acceptance are estimated by varying the shapes introducing functional dependences that would bias the angular observables.

	Uncorrected values	Corrected values
F_L	0.15 ± 0.06	$0.16 \pm 0.06 \pm 0.03$
$A_T^{(2)}$	-0.22 ± 0.23	$-0.23 \pm 0.23 \pm 0.05$
A_T^{Im}	$+0.14 \pm 0.22$	$+0.14 \pm 0.22 \pm 0.05$
A_T^{Re}	$+0.09 \pm 0.18$	$+0.10 \pm 0.18 \pm 0.05$

Table 1: Fit results for the angular observables F_L , $A_T^{(2)}$, A_T^{Im} and A_T^{Re} . The second column corresponds to the uncorrected values directly obtained from the fit while the third column gives the final results after the correction for the $(3.8 \pm 1.9)\%$ of $B^0 \rightarrow K^{*0} \gamma e^+ e^-$ contamination and for the small fit biases due to the limited size of the data sample. The first uncertainty is statistical and the second systematic.

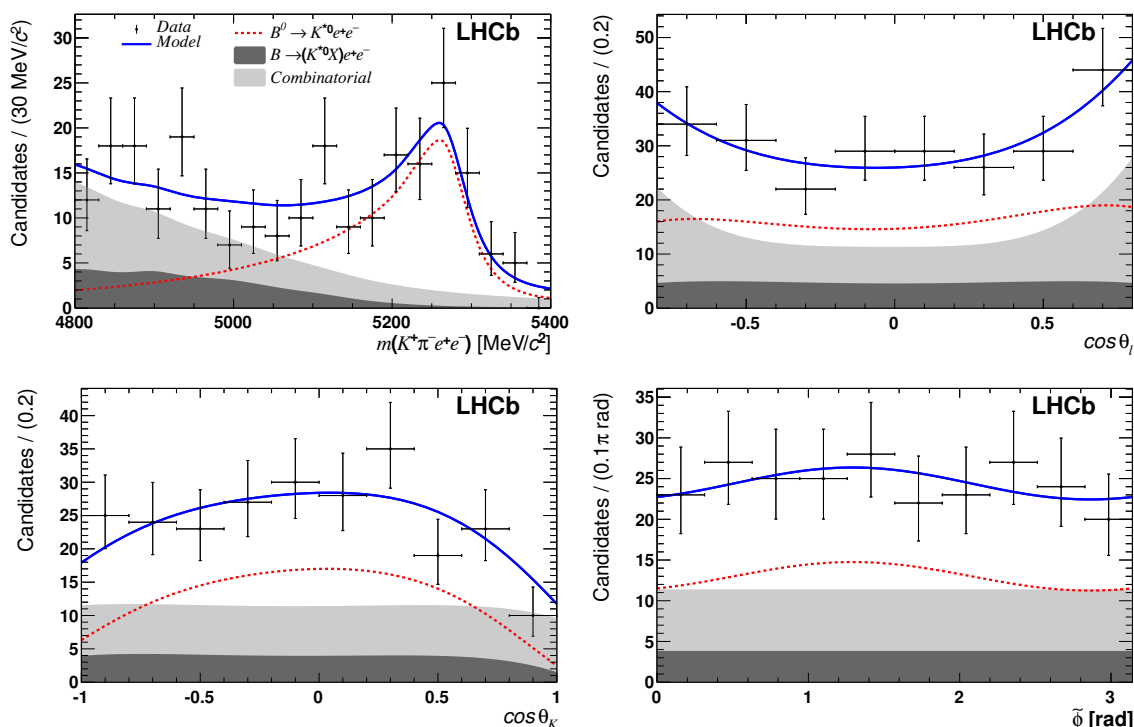


Figure 4: Distributions of the $K^+ \pi^- e^+ e^-$ invariant mass, $\cos \theta_\ell$, $\cos \theta_K$ and $\tilde{\phi}$ variables for the $B^0 \rightarrow K^{*0} e^+ e^-$ decay mode and the three trigger categories grouped together. The dashed line is the signal PDF, the light grey area corresponds to the combinatorial background, the dark grey area is the PR background. The solid line is the total PDF.

The uncertainties due to the description of the shape of the combinatorial background are obtained from the uncertainties on the parameters describing the shapes and by allowing for potential $\cos 2\tilde{\phi}$ and $\sin 2\tilde{\phi}$ modulations.

To estimate the uncertainties due to the modelling of the PR background the $F_{L,PR}$ parameter is varied between 0.17 and 0.5. The systematic uncertainties related to the $A_T^{(2)}$ and A_T^{Im} observables depend on the values of the observables themselves: their sizes are assessed by varying the damping factor up to 0.5, i.e. reducing the distortions of the $\tilde{\phi}$

Source	$\sigma(F_L)$	$\sigma(A_T^{(2)})$	$\sigma(A_T^{\text{Im}})$	$\sigma(A_T^{\text{Re}})$
Acceptance modelling	0.013	0.038	0.035	0.031
Combinatorial background	0.006	0.030	0.029	0.038
PR background	0.019	0.011	0.007	0.009
$B^0 \rightarrow K^{*0}\gamma$ contamination	0.003	0.004	0.003	0.002
Fit bias	0.008	-	-	0.010
Total systematic uncertainty	0.03	0.05	0.05	0.05
Statistical uncertainty	0.06	0.23	0.22	0.18

Table 2: Summary of the systematic uncertainties.

distribution of the PR background by a factor of two compared to the signal ones. For the A_T^{Re} parameter, the systematic uncertainty is estimated by varying $A_{T,\text{PR}}^{\text{Re}}$ up to the fitted value obtained for $B^0 \rightarrow K^{*0}e^+e^-$.

The systematic uncertainties from the $B^0 \rightarrow K^{*0}\gamma_{e^+e^-}$ background are due to the uncertainty on the size of the contamination.

Finally, to estimate possible biases due to the fitting procedure, a large number of pseudo-experiments are generated with the number of events observed in data and are fitted with the default PDFs. While the $A_T^{(2)}$ and A_T^{Im} estimates are not biased, the F_L and A_T^{Re} observables exhibit small biases (less than 10% of the statistical uncertainties) due to the limited size of the data sample and are corrected accordingly. The values of the corrections are assigned as uncertainties (labelled as ‘‘Fit bias’’ in table 2).

The systematic uncertainties are summarised in table 2. The systematic uncertainties on the F_L , $A_T^{(2)}$, A_T^{Im} and A_T^{Re} angular observables in table 1 are obtained by adding these contributions in quadrature. They are, in all cases, smaller than the statistical uncertainties.

7.3 Effective q^2 range of the selected $B^0 \rightarrow K^{*0}e^+e^-$ signal events

The distribution of the reconstructed q^2 for the signal is obtained using the *sPlot* technique [42] based on the B^0 invariant mass spectrum and shown in figure 5. Taking into account the effect of event migration in and out the q^2 bin, the average value of the true q^2 of the selected signal events is equal to $q^2 = 0.17 \pm 0.04 \text{ GeV}^2/c^4$. The acceptance as a function of the true q^2 , obtained from the LHCb simulation, is uniform in a large domain except close to the limits of the reconstructed q^2 , 0.0004 and $1 \text{ GeV}^2/c^4$. Due to reconstruction effects, the q^2 effective limits are slightly different. Because of reduced acceptance in the low- q^2 region, the value of the lower q^2 effective limit is increased; because of bremsstrahlung radiation, events with a true q^2 greater than $1 \text{ GeV}^2/c^4$ are accepted by the selection and the higher q^2 effective limit is also increased. The values of these effective boundaries are obtained by requiring that in the low- and high- q^2 regions the same number of events are obtained in a uniform acceptance model and in the LHCb simulation. The true q^2 effective region is thus determined to be between 0.002 and $1.12 \text{ GeV}^2/c^4$. It is checked, using the LHCb simulation, that the average values of the true q^2 and of the angular observables evaluated with a uniform acceptance in the region between 0.002 and $1.12 \text{ GeV}^2/c^4$ are in agreement with those obtained from the angular fit performed on the events selected in

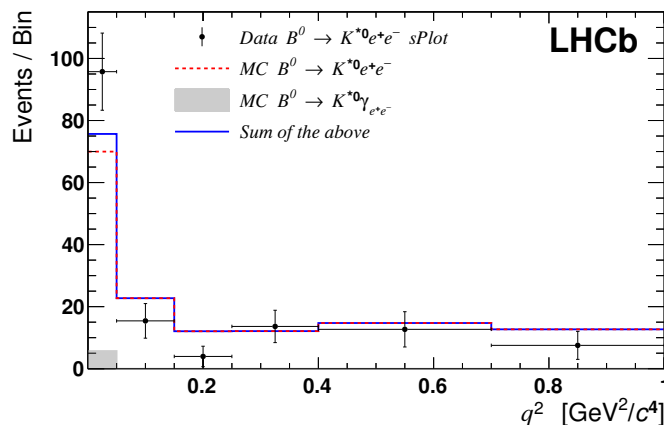


Figure 5: Distribution of the reconstructed q^2 from an *sPlot* of data (black points). The dashed line represents the $B^0 \rightarrow K^{*0} e^+ e^-$ contribution and the grey area corresponds to the 3.8% $B^0 \rightarrow K^{*0} \gamma_{e^+ e^-}$ contamination. The solid line is the sum of the two.

the reconstructed q^2 interval 0.0004 to 1 GeV^2/c^4 . An uncertainty on the q^2 effective limits is assigned as half of the q^2 limit modification. The true q^2 effective range is thus from 0.0020 ± 0.0008 to $1.120 \pm 0.060 \text{ GeV}^2/c^4$. This range should be used to compare the F_L , $A_T^{(2)}$, A_T^{Im} and A_T^{Re} measurements with predictions.

8 Summary

An angular analysis of the $B^0 \rightarrow K^{*0} e^+ e^-$ decay is performed using proton-proton collision data, corresponding to an integrated luminosity of 3.0 fb^{-1} , collected by the LHCb experiment in 2011 and 2012. Angular observables are measured for the first time in an effective q^2 range from 0.0020 ± 0.0008 to $1.120 \pm 0.060 \text{ GeV}^2/c^4$. The results are

$$\begin{aligned}
 F_L &= 0.16 \pm 0.06 \pm 0.03 \\
 A_T^{(2)} &= -0.23 \pm 0.23 \pm 0.05 \\
 A_T^{\text{Im}} &= +0.14 \pm 0.22 \pm 0.05 \\
 A_T^{\text{Re}} &= +0.10 \pm 0.18 \pm 0.05,
 \end{aligned}$$

where the first contribution to the uncertainty is statistical and the second systematic. The results are consistent with SM predictions [2, 43]. For the low average value of q^2 of this analysis, the formulae relating $A_T^{(2)}$ and A_T^{Im} and \mathcal{C}_7 and \mathcal{C}'_7 in eq. 1.3 are accurate at the 5% level, for SM values of the ratios of Wilson coefficients $\mathcal{C}_9/\mathcal{C}_7$ and $\mathcal{C}_{10}/\mathcal{C}_7$. At this level of precision and for SM values of \mathcal{C}_7 , the ratio $\mathcal{C}'_7/\mathcal{C}_7$ is compatible with zero. This determination is more precise than that obtained from the average of the time-dependent measurements of CP asymmetry in $B^0 \rightarrow K^{*0} (\rightarrow K_S^0 \pi^0) \gamma$ decays [16, 17].

Acknowledgments

We express our gratitude to our colleagues in the CERN accelerator departments for the excellent performance of the LHC. We thank the technical and administrative staff at the LHCb institutes. We acknowledge support from CERN and from the national agencies: CAPES, CNPq, FAPERJ and FINEP (Brazil); NSFC (China); CNRS/IN2P3 (France); BMBF, DFG, HGF and MPG (Germany); INFN (Italy); FOM and NWO (The Netherlands); MNiSW and NCN (Poland); MEN/IFA (Romania); MinES and FANO (Russia); MinECo (Spain); SNSF and SER (Switzerland); NASU (Ukraine); STFC (United Kingdom); NSF (USA). The Tier1 computing centres are supported by IN2P3 (France), KIT and BMBF (Germany), INFN (Italy), NWO and SURF (The Netherlands), PIC (Spain), GridPP (United Kingdom). We are indebted to the communities behind the multiple open source software packages on which we depend. We are also thankful for the computing resources and the access to software R&D tools provided by Yandex LLC (Russia). Individual groups or members have received support from EPLANET, Marie Skłodowska-Curie Actions and ERC (European Union), Conseil général de Haute-Savoie, Labex ENIGMASS and OCEVU, Région Auvergne (France), RFBR (Russia), XuntaGal and GENCAT (Spain), Royal Society and Royal Commission for the Exhibition of 1851 (United Kingdom).

Open Access. This article is distributed under the terms of the Creative Commons Attribution License ([CC-BY 4.0](https://creativecommons.org/licenses/by/4.0/)), which permits any use, distribution and reproduction in any medium, provided the original author(s) and source are credited.

References

- [1] F. Krüger and J. Matias, *Probing new physics via the transverse amplitudes of $B^0 \rightarrow K^{*0}(\rightarrow K^+\pi^-)$ at large recoil*, *Phys. Rev. D* **71** (2005) 094009 [[hep-ph/0502060](#)] [[INSPIRE](#)].
- [2] D. Becirevic and E. Schneider, *On transverse asymmetries in $B \rightarrow K^*\ell^+\ell^-$* , *Nucl. Phys. B* **854** (2012) 321 [[arXiv:1106.3283](#)] [[INSPIRE](#)].
- [3] Y. Grossman and D. Pirjol, *Extracting and using photon polarization information in radiative B decays*, *JHEP* **06** (2000) 029 [[hep-ph/0005069](#)] [[INSPIRE](#)].
- [4] S. Jäger and J. Martin Camalich, *On $B \rightarrow V\ell\ell$ at small dilepton invariant mass, power corrections and new physics*, *JHEP* **05** (2013) 043 [[arXiv:1212.2263](#)] [[INSPIRE](#)].
- [5] L.L. Everett, G.L. Kane, S. Rigolin, L.-T. Wang and T.T. Wang, *Alternative approach to $b \rightarrow s\gamma$ in the $uMSSM$* , *JHEP* **01** (2002) 022 [[hep-ph/0112126](#)] [[INSPIRE](#)].
- [6] J. Foster, K.-i. Okumura and L. Roszkowski, *New Constraints on SUSY Flavour Mixing in Light of Recent Measurements at the Tevatron*, *Phys. Lett. B* **641** (2006) 452 [[hep-ph/0604121](#)] [[INSPIRE](#)].
- [7] E. Lunghi and J. Matias, *Huge right-handed current effects in $B \rightarrow K^{*0}(K\pi)\ell^+\ell^-$ in supersymmetry*, *JHEP* **04** (2007) 058 [[hep-ph/0612166](#)] [[INSPIRE](#)].
- [8] T. Goto, Y. Okada, T. Shindou and M. Tanaka, *Patterns of flavor signals in supersymmetric models*, *Phys. Rev. D* **77** (2008) 095010 [[arXiv:0711.2935](#)] [[INSPIRE](#)].

- [9] CDF collaboration, T. Aaltonen et al., *Measurements of the Angular Distributions in the Decays $B \rightarrow K^{(*)}\mu^+\mu^-$ at CDF*, *Phys. Rev. Lett.* **108** (2012) 081807 [[arXiv:1108.0695](#)] [[INSPIRE](#)].
- [10] LHCb collaboration, *Differential branching fraction and angular analysis of the decay $B^0 \rightarrow K^{*0}\mu^+\mu^-$* , *JHEP* **08** (2013) 131 [[arXiv:1304.6325](#)] [[INSPIRE](#)].
- [11] J.-T. Wei et al., *Measurement of the Differential Branching Fraction and Forward-Backward Asymmetry for $B \rightarrow K^{(*)}l^+l^-$* , *Phys. Rev. Lett.* **103** (2009) 171801.
- [12] J. Lefrançois and M.H. Schune, *Measuring the photon polarization in $b \rightarrow s\gamma$ using the $B^0 \rightarrow K^{*0}e^+e^-$ decay channel*, LHCb-PUB-2009-008 (2009).
- [13] LHCb collaboration, *Measurement of the $B^0 \rightarrow K^{*0}e^+e^-$ branching fraction at low dilepton mass*, *JHEP* **05** (2013) 159 [[arXiv:1304.3035](#)] [[INSPIRE](#)].
- [14] C.-D. Lu and W. Wang, *Analysis of $B \rightarrow K_J^*(\rightarrow K\pi)\mu^+\mu^-$ in the higher kaon resonance region*, *Phys. Rev. D* **85** (2012) 034014 [[arXiv:1111.1513](#)] [[INSPIRE](#)].
- [15] C. Bobeth, G. Hiller and G. Piranishvili, *CP Asymmetries in $\bar{B} \rightarrow \bar{K}^*(\rightarrow \bar{K}\pi)\bar{\ell}\ell$ and Untagged $\bar{B}_s, B_s \rightarrow \phi(\rightarrow K^+K^-)\bar{\ell}\ell$ Decays at NLO*, *JHEP* **07** (2008) 106 [[arXiv:0805.2525](#)] [[INSPIRE](#)].
- [16] BaBar collaboration, B. Aubert et al., *Measurement of Time-Dependent CP Asymmetry in $B^0 \rightarrow K_S^0\pi^0\gamma$ Decays*, *Phys. Rev. D* **78** (2008) 071102 [[arXiv:0807.3103](#)] [[INSPIRE](#)].
- [17] BELLE collaboration, Y. Ushiroda et al., *Time-Dependent CP Asymmetries in $B^0 \rightarrow K_S^0\pi^0\gamma$ transitions*, *Phys. Rev. D* **74** (2006) 111104 [[hep-ex/0608017](#)] [[INSPIRE](#)].
- [18] LHCb collaboration, *The LHCb Detector at the LHC*, 2008 *JINST* **3** S08005 [[INSPIRE](#)].
- [19] LHCb collaboration, *LHCb Detector Performance*, *Int. J. Mod. Phys. A* **30** (2015) 1530022 [[arXiv:1412.6352](#)] [[INSPIRE](#)].
- [20] R. Aaij et al., *Performance of the LHCb Vertex Locator*, 2014 *JINST* **9** 09007 [[arXiv:1405.7808](#)] [[INSPIRE](#)].
- [21] LHCb Outer Tracker Group collaboration, R. Arink et al., *Performance of the LHCb Outer Tracker*, 2014 *JINST* **9** P01002 [[arXiv:1311.3893](#)] [[INSPIRE](#)].
- [22] LHCb RICH Group collaboration, M. Adinolfi et al., *Performance of the LHCb RICH detector at the LHC*, *Eur. Phys. J. C* **73** (2013) 2431 [[arXiv:1211.6759](#)] [[INSPIRE](#)].
- [23] A.A. Alves Jr. et al., *Performance of the LHCb muon system*, 2013 *JINST* **8** P02022 [[arXiv:1211.1346](#)] [[INSPIRE](#)].
- [24] R. Aaij et al., *The LHCb Trigger and its Performance in 2011*, 2013 *JINST* **8** P04022 [[arXiv:1211.3055](#)] [[INSPIRE](#)].
- [25] V.V. Gligorov and M. Williams, *Efficient, reliable and fast high-level triggering using a bonsai boosted decision tree*, 2013 *JINST* **8** P02013 [[arXiv:1210.6861](#)] [[INSPIRE](#)].
- [26] T. Sjöstrand, S. Mrenna and P.Z. Skands, *PYTHIA 6.4 Physics and Manual*, *JHEP* **05** (2006) 026 [[hep-ph/0603175](#)] [[INSPIRE](#)].
- [27] T. Sjöstrand, S. Mrenna and P.Z. Skands, *A Brief Introduction to PYTHIA 8.1*, *Comput. Phys. Commun.* **178** (2008) 852 [[arXiv:0710.3820](#)] [[INSPIRE](#)].
- [28] I. Belyaev et al., *Handling of the generation of primary events in Gauss, the LHCb simulation framework*, *IEEE Nucl. Sci. Symp. Conf. Rec. (NSS/MIC)* (2010) 1155.

- [29] D.J. Lange, *The EvtGen particle decay simulation package*, *Nucl. Instrum. Meth. A* **462** (2001) 152 [INSPIRE].
- [30] P. Golonka and Z. Was, *PHOTOS Monte Carlo: A Precision tool for QED corrections in Z and W decays*, *Eur. Phys. J. C* **45** (2006) 97 [hep-ph/0506026] [INSPIRE].
- [31] GEANT4 collaboration, J. Allison et al., *Geant4 developments and applications*, *IEEE Trans. Nucl. Sci.* **53** (2006) 270.
- [32] GEANT4 collaboration, S. Agostinelli et al., *Geant4: A Simulation toolkit*, *Nucl. Instrum. Meth. A* **506** (2003) 250 [INSPIRE].
- [33] M. Clemencic et al., *The LHCb simulation application, Gauss: Design, evolution and experience*, *J. Phys. Conf. Ser.* **331** (2011) 032023 [INSPIRE].
- [34] L. Breiman, J.H. Friedman, R.A. Olshen and C.J. Stone, *Classification and regression trees*, Wadsworth international group, Belmont, California U.S.A. (1984)
- [35] R.E. Schapire and Y. Freund, *A decision-theoretic generalization of on-line learning and an application to boosting*, *J. Comp. Syst. Sc.* **55** (1997) 119.
- [36] CDF collaboration, A. Abulencia et al., *Search for $B_s \rightarrow \mu^+ \mu^-$ and $B_d \rightarrow \mu^+ \mu^-$ decays in $p\bar{p}$ collisions with CDF II*, *Phys. Rev. Lett.* **95** (2005) 221805 [Erratum *ibid.* **95** (2005) 249905] [hep-ex/0508036] [INSPIRE].
- [37] A. Borsellino, *Momentum Transfer and Angle of Divergence of Pairs Produced by Photons*, *Phys. Rev.* **89** (1953) 1023 [INSPIRE].
- [38] A.Y. Korchin and V.A. Kovalchuk, *Contribution of low-lying vector resonances to polarization observables in $B^0 \rightarrow K^{*0} e^+ e^-$ decay*, *Phys. Rev. D* **82** (2010) 034013 [arXiv:1004.3647] [INSPIRE].
- [39] LHCb collaboration, *Test of lepton universality using $B^+ \rightarrow K^+ \ell^+ \ell^-$ decays*, *Phys. Rev. Lett.* **113** (2014) 151601 [arXiv:1406.6482] [INSPIRE].
- [40] T. Skwarnicki, *A study of the radiative cascade transitions between the Upsilon-prime and Upsilon resonances*, PhD thesis, Institute of Nuclear Physics, Krakow (1986) DESY-F31-86-02.
- [41] K.S. Cranmer, *Kernel estimation in high-energy physics*, *Comput. Phys. Commun.* **136** (2001) 198 [hep-ex/0011057] [INSPIRE].
- [42] M. Pivk and F.R. Le Diberder, *SPlot: A Statistical tool to unfold data distributions*, *Nucl. Instrum. Meth. A* **555** (2005) 356 [physics/0402083] [INSPIRE].
- [43] S. Jäger and J. Martin Camalich, *Reassessing the discovery potential of the $B \rightarrow K^* \ell^+ \ell^-$ decays in the large-recoil region: SM challenges and BSM opportunities*, arXiv:1412.3183 [INSPIRE].

The LHCb collaboration

R. Aaij⁴¹, B. Adeva³⁷, M. Adinolfi⁴⁶, A. Affolder⁵², Z. Ajaltouni⁵, S. Akar⁶, J. Albrecht⁹, F. Alessio³⁸, M. Alexander⁵¹, S. Ali⁴¹, G. Alkhazov³⁰, P. Alvarez Cartelle³⁷, A.A. Alves Jr^{25,38}, S. Amato², S. Amerio²², Y. Amhis⁷, L. An³, L. Anderlini^{17,g}, J. Anderson⁴⁰, R. Andreassen⁵⁷, M. Andreotti^{16,f}, J.E. Andrews⁵⁸, R.B. Appleby⁵⁴, O. Aquines Gutierrez¹⁰, F. Archilli³⁸, A. Artamonov³⁵, M. Artuso⁵⁹, E. Aslanides⁶, G. Auriemma^{25,n}, M. Baalouch⁵, S. Bachmann¹¹, J.J. Back⁴⁸, A. Badalov³⁶, C. Baesso⁶⁰, W. Baldini¹⁶, R.J. Barlow⁵⁴, C. Barschel³⁸, S. Barsuk⁷, W. Barter³⁸, V. Batozskaya²⁸, V. Battista³⁹, A. Bay³⁹, L. Beaucourt⁴, J. Beddow⁵¹, F. Bedeschi²³, I. Bediaga¹, S. Belogurov³¹, I. Belyaev³¹, E. Ben-Haim⁸, G. Bencivenni¹⁸, S. Benson³⁸, J. Benton⁴⁶, A. Berezhnoy³², R. Bernet⁴⁰, A. Bertolin²², M.-O. Bettler⁴⁷, M. van Beuzekom⁴¹, A. Bien¹¹, S. Bifani⁴⁵, T. Bird⁵⁴, A. Bizzeti^{17,i}, T. Blake⁴⁸, F. Blanc³⁹, J. Blouw¹⁰, S. Blusk⁵⁹, V. Bocci²⁵, A. Bondar³⁴, N. Bondar^{30,38}, W. Bonivento¹⁵, S. Borghi⁵⁴, A. Borgia⁵⁹, M. Borsato⁷, T.J.V. Bowcock⁵², E. Bowen⁴⁰, C. Bozzi¹⁶, D. Brett⁵⁴, M. Britsch¹⁰, T. Britton⁵⁹, J. Brodzicka⁵⁴, N.H. Brook⁴⁶, A. Bursche⁴⁰, J. Buytaert³⁸, S. Cadeddu¹⁵, R. Calabrese^{16,f}, M. Calvi^{20,k}, M. Calvo Gomez^{36,p}, P. Campana¹⁸, D. Campora Perez³⁸, L. Capriotti⁵⁴, A. Carbone^{14,d}, G. Carboni^{24,l}, R. Cardinale^{19,38,j}, A. Cardini¹⁵, L. Carson⁵⁰, K. Carvalho Akiba^{2,38}, RCM Casanova Mohr³⁶, G. Casse⁵², L. Cassina^{20,k}, L. Castillo Garcia³⁸, M. Cattaneo³⁸, Ch. Cauet⁹, R. Cenci^{23,t}, M. Charles⁸, Ph. Charpentier³⁸, M. Chefdeville⁴, S. Chen⁵⁴, S.-F. Cheung⁵⁵, N. Chiapolini⁴⁰, M. Chruszcz^{40,26}, X. Cid Vidal³⁸, G. Ciezarek⁴¹, P.E.L. Clarke⁵⁰, M. Clemencic³⁸, H.V. Cliff⁴⁷, J. Closier³⁸, V. Coco³⁸, J. Cogan⁶, E. Cogneras⁵, V. Cogoni^{15,e}, L. Cojocariu²⁹, G. Collazuol²², P. Collins³⁸, A. Comerma-Montells¹¹, A. Contu^{15,38}, A. Cook⁴⁶, M. Coombes⁴⁶, S. Coquereau⁸, G. Corti³⁸, M. Corvo^{16,f}, I. Counts⁵⁶, B. Couturier³⁸, G.A. Cowan⁵⁰, D.C. Craik⁴⁸, A.C. Crocombe⁴⁸, M. Cruz Torres⁶⁰, S. Cunliffe⁵³, R. Currie⁵³, C. D'Ambrosio³⁸, J. Dalseno⁴⁶, P. David⁸, P.N.Y. David⁴¹, A. Davis⁵⁷, K. De Bruyn⁴¹, S. De Capua⁵⁴, M. De Cian¹¹, J.M. De Miranda¹, L. De Paula², W. De Silva⁵⁷, P. De Simone¹⁸, C.-T. Dean⁵¹, D. Decamp⁴, M. Deckenhoff⁹, L. Del Buono⁸, N. Déléage⁴, D. Derkach⁵⁵, O. Deschamps⁵, F. Dettori³⁸, B. Dey⁴⁰, A. Di Canto³⁸, A. Di Domenico²⁵, F. Di Ruscio²⁴, H. Dijkstra³⁸, S. Donleavy⁵², F. Dordei¹¹, M. Dorigo³⁹, A. Dosil Suárez³⁷, D. Dossett⁴⁸, A. Dovbnya⁴³, K. Dreimanis⁵², G. Dujany⁵⁴, F. Dupertuis³⁹, P. Durante⁶, R. Dzhelyadin³⁵, A. Dziurda²⁶, A. Dzyuba³⁰, S. Easo^{49,38}, U. Egede⁵³, V. Egorychev³¹, S. Eidelman³⁴, S. Eisenhardt⁵⁰, U. Eitschberger⁹, R. Ekelhof⁹, L. Eklund⁵¹, I. El Rifai⁵, Ch. Elsasser⁴⁰, S. Ely⁵⁹, S. Esen¹¹, H.M. Evans⁴⁷, T. Evans⁵⁵, A. Falabella¹⁴, C. Färber¹¹, C. Farinelli⁴¹, N. Farley⁴⁵, S. Farry⁵², R. Fay⁵², D. Ferguson⁵⁰, V. Fernandez Albor³⁷, F. Ferreira Rodrigues¹, M. Ferro-Luzzi³⁸, S. Filippov³³, M. Fiore^{16,f}, M. Fiorini^{16,f}, M. Firlej²⁷, C. Fitzpatrick³⁹, T. Fiutowski²⁷, P. Fol⁵³, M. Fontana¹⁰, F. Fontanelli^{19,j}, R. Forty³⁸, O. Francisco², M. Frank³⁸, C. Frei³⁸, M. Frosini¹⁷, J. Fu^{21,38}, E. Furfaro^{24,l}, A. Gallas Torreira³⁷, D. Galli^{14,d}, S. Gallorini^{22,38}, S. Gambetta^{19,j}, M. Gandelman², P. Gandini⁵⁹, Y. Gao³, J. García Pardiñas³⁷, J. Garofoli⁵⁹, J. Garra Tico⁴⁷, L. Garrido³⁶, D. Gascon³⁶, C. Gaspar³⁸, U. Gastaldi¹⁶, R. Gauld⁵⁵, L. Gavardi⁹, G. Gazzoni⁵, A. Geraci^{21,v}, E. Gersabeck¹¹, M. Gersabeck⁵⁴, T. Gershon⁴⁸, Ph. Ghez⁴, A. Gianelle²², S. Giani³⁹, V. Gibson⁴⁷, L. Giubega²⁹, V.V. Gligorov³⁸, C. Göbel⁶⁰, D. Golubkov³¹, A. Golutvin^{53,31,38}, A. Gomes^{1,a}, C. Gotti^{20,k}, M. Grabalosa Gándara⁵, R. Graciani Diaz³⁶, L.A. Granado Cardoso³⁸, E. Graugés³⁶, E. Graverini⁴⁰, G. Graziani¹⁷, A. Grecu²⁹, E. Greening⁵⁵, S. Gregson⁴⁷, P. Griffith⁴⁵, L. Grillo¹¹, O. Grünberg⁶³, B. Gui⁵⁹, E. Gushchin³³, Yu. Guz^{35,38}, T. Gys³⁸, C. Hadjivasiliou⁵⁹, G. Haefeli³⁹, C. Haen³⁸, S.C. Haines⁴⁷, S. Hall⁵³, B. Hamilton⁵⁸, T. Hampson⁴⁶, X. Han¹¹, S. Hansmann-Menzemer¹¹, N. Harnew⁵⁵, S.T. Harnew⁴⁶, J. Harrison⁵⁴, J. He³⁸, T. Head³⁹, V. Heijne⁴¹, K. Hennessy⁵², P. Henrard⁵, L. Henry⁸, J.A. Hernando Morata³⁷, E. van Herwijnen³⁸, M. Heß⁶³, A. Hicheur², D. Hill⁵⁵, M. Hoballah⁵, C. Hombach⁵⁴,

W. Hulsbergen⁴¹, N. Hussain⁵⁵, D. Hutchcroft⁵², D. Hynds⁵¹, M. Idzik²⁷, P. Ilten⁵⁶, R. Jacobsson³⁸, A. Jaeger¹¹, J. Jalocho⁵⁵, E. Jans⁴¹, A. Jawahery⁵⁸, F. Jing³, M. John⁵⁵, D. Johnson³⁸, C.R. Jones⁴⁷, C. Joram³⁸, B. Jost³⁸, N. Jurik⁵⁹, S. Kandybei⁴³, W. Kanso⁶, M. Karacson³⁸, T.M. Karbach³⁸, S. Karodia⁵¹, M. Kelsey⁵⁹, I.R. Kenyon⁴⁵, M. Kenzie³⁸, T. Ketel⁴², B. Khanji^{20,38,k}, C. Khurewathanakul³⁹, S. Klaver⁵⁴, K. Klimaszewski²⁸, O. Kochebina⁷, M. Kolpin¹¹, I. Komarov³⁹, R.F. Koopman⁴², P. Koppenburg^{41,38}, M. Korolev³², L. Kravchuk³³, K. Kreplin¹¹, M. Krepis⁴⁸, G. Krocker¹¹, P. Krokovny³⁴, F. Kruse⁹, W. Kucewicz^{26,o}, M. Kucharczyk^{20,26,k}, V. Kudryavtsev³⁴, K. Kurek²⁸, T. Kvaratskheliya³¹, V.N. La Thi³⁹, D. Lacarrere³⁸, G. Lafferty⁵⁴, A. Lai¹⁵, D. Lambert⁵⁰, R.W. Lambert⁴², G. Lanfranchi¹⁸, C. Langenbruch⁴⁸, B. Langhans³⁸, T. Latham⁴⁸, C. Lazzeroni⁴⁵, R. Le Gac⁶, J. van Leerdam⁴¹, J.-P. Lees⁴, R. Lefèvre⁵, A. Leflat³², J. Lefrançois⁷, O. Leroy⁶, T. Lesiak²⁶, B. Leverington¹¹, Y. Li⁷, T. Likhomanenko⁶⁴, M. Liles⁵², R. Lindner³⁸, C. Linn³⁸, F. Lionetto⁴⁰, B. Liu¹⁵, S. Lohn³⁸, I. Longstaff⁵¹, J.H. Lopes², P. Lowdon⁴⁰, D. Lucchesi^{22,r}, H. Luo⁵⁰, A. Lupato²², E. Luppi^{16,f}, O. Lupton⁵⁵, F. Machefert⁷, I.V. Machikhiliyan³¹, F. Maciuc²⁹, O. Maev³⁰, S. Malde⁵⁵, A. Malinin⁶⁴, G. Manca^{15,e}, G. Mancinelli⁶, P. Manning⁵⁹, A. Mapelli³⁸, J. Maratas⁵, J.F. Marchand⁴, U. Marconi¹⁴, C. Marin Benito³⁶, P. Marino^{23,t}, R. Märki³⁹, J. Marks¹¹, G. Martellotti²⁵, M. Martinelli³⁹, D. Martinez Santos⁴², F. Martinez Vidal⁶⁵, D. Martins Tostes², A. Massafferri¹, R. Matev³⁸, Z. Mathe³⁸, C. Matteuzzi²⁰, B. Maurin³⁹, A. Mazurov⁴⁵, M. McCann⁵³, J. McCarthy⁴⁵, A. McNab⁵⁴, R. McNulty¹², B. McKelley⁵², B. Meadows⁵⁷, F. Meier⁹, M. Meissner¹¹, M. Merk⁴¹, D.A. Milanes⁶², M.-N. Minard⁴, N. Moggi¹⁴, J. Molina Rodriguez⁶⁰, S. Monteil⁵, M. Morandin²², P. Morawski²⁷, A. Mordà⁶, M.J. Morello^{23,t}, J. Moron²⁷, A.-B. Morris⁵⁰, R. Mountain⁵⁹, F. Muheim⁵⁰, K. Müller⁴⁰, M. Mussini¹⁴, B. Muster³⁹, P. Naik⁴⁶, T. Nakada³⁹, R. Nandakumar⁴⁹, I. Nasteva², M. Needham⁵⁰, N. Neri²¹, S. Neubert³⁸, N. Neufeld³⁸, M. Neuner¹¹, A.D. Nguyen³⁹, T.D. Nguyen³⁹, C. Nguyen-Mau^{39,q}, M. Nicol⁷, V. Niess⁵, R. Niet⁹, N. Nikitin³², T. Nikodem¹¹, A. Novoselov³⁵, D.P. O’Hanlon⁴⁸, A. Oblakowska-Mucha²⁷, V. Obraztsov³⁵, S. Ogilvy⁵¹, O. Okhrimenko⁴⁴, R. Oldeman^{15,e}, C.J.G. Onderwater⁶⁶, M. Orlandea²⁹, B. Osorio Rodrigues¹, J.M. Otalora Goicochea², A. Otto³⁸, P. Owen⁵³, A. Oyanguren⁶⁵, B.K. Pal⁵⁹, A. Palano^{13,c}, F. Palombo^{21,u}, M. Palutan¹⁸, J. Panman³⁸, A. Papanestis^{49,38}, M. Pappagallo⁵¹, L.L. Pappalardo^{16,f}, C. Parkes⁵⁴, C.J. Parkinson^{9,45}, G. Passaleva¹⁷, G.D. Patel⁵², M. Patel⁵³, C. Patrignani^{19,j}, A. Pearce^{54,49}, A. Pellegrino⁴¹, G. Penso^{25,m}, M. Pepe Altarelli³⁸, S. Perazzini^{14,d}, P. Perret⁵, L. Pescatore⁴⁵, E. Pesen⁶⁷, K. Petridis⁴⁶, A. Petrolini^{19,j}, E. Picatoste Olloqui³⁶, B. Pietrzyk⁴, T. Pilar⁴⁸, D. Pinci²⁵, A. Pistone¹⁹, S. Playfer⁵⁰, M. Plo Casasus³⁷, F. Polci⁸, A. Poluektov^{48,34}, I. Polyakov³¹, E. Polcarpo², A. Popov³⁵, D. Popov¹⁰, B. Popovici²⁹, C. Potterat², E. Price⁴⁶, J.D. Price⁵², J. Prisciandaro³⁹, A. Pritchard⁵², C. Prouve⁴⁶, V. Pugatch⁴⁴, A. Puig Navarro³⁹, G. Punzi^{23,s}, W. Qian⁴, R. Quagliani^{7,46}, B. Rachwal²⁶, J.H. Rademacker⁴⁶, B. Rakotomiarimana³⁹, M. Rama²³, M.S. Rangel², I. Raniuk⁴³, N. Rauschmayr³⁸, G. Raven⁴², F. Redi⁵³, S. Reichert⁵⁴, M.M. Reid⁴⁸, A.C. dos Reis¹, S. Ricciardi⁴⁹, S. Richards⁴⁶, M. Rihl³⁸, K. Rinnert⁵², V. Rives Molina³⁶, P. Robbe⁷, A.B. Rodrigues¹, E. Rodrigues⁵⁴, P. Rodriguez Perez⁵⁴, S. Roiser³⁸, V. Romanovsky³⁵, A. Romero Vidal³⁷, M. Rotondo²², J. Rouvinet³⁹, T. Ruf³⁸, H. Ruiz³⁶, P. Ruiz Valls⁶⁵, J.J. Saborido Silva³⁷, N. Sagidova³⁰, P. Sail⁵¹, B. Saitta^{15,e}, V. Salustino Guimaraes², C. Sanchez Mayordomo⁶⁵, B. Sanmartin Sedes³⁷, R. Santacesaria²⁵, C. Santamarina Rios³⁷, E. Santovetti^{24,l}, A. Sarti^{18,m}, C. Satriano^{25,n}, A. Satta²⁴, D.M. Saunders⁴⁶, D. Savrina^{31,32}, M. Schiller³⁸, H. Schindler³⁸, M. Schlupp⁹, M. Schmelling¹⁰, B. Schmidt³⁸, O. Schneider³⁹, A. Schopper³⁸, M.-H. Schune⁷, R. Schwemmer³⁸, B. Sciascia¹⁸, A. Sciubba^{25,m}, A. Semennikov³¹, I. Sepp⁵³, N. Serra⁴⁰, J. Serrano⁶, L. Sestini²², P. Seyfert¹¹, M. Shapkin³⁵, I. Shapoval^{16,43,f}, Y. Shcheglov³⁰, T. Shears⁵², L. Shekhtman³⁴, V. Shevchenko⁶⁴, A. Shires⁹, R. Silva Coutinho⁴⁸, G. Simi²², M. Sirendi⁴⁷, N. Skidmore⁴⁶, I. Skillicorn⁵¹, T. Skwarnicki⁵⁹,

N.A. Smith⁵², E. Smith^{55,49}, E. Smith⁵³, J. Smith⁴⁷, M. Smith⁵⁴, H. Snoek⁴¹, M.D. Sokoloff⁵⁷, F.J.P. Soler⁵¹, F. Soomro³⁹, D. Souza⁴⁶, B. Souza De Paula², B. Spaan⁹, P. Spradlin⁵¹, S. Sridharan³⁸, F. Stagni³⁸, M. Stahl¹¹, S. Stahl³⁸, O. Steinkamp⁴⁰, O. Stenyakin³⁵, F. Sterpka⁵⁹, S. Stevenson⁵⁵, S. Stoica²⁹, S. Stone⁵⁹, B. Storaci⁴⁰, S. Stracka^{23,t}, M. Straticiuc²⁹, U. Straumann⁴⁰, R. Stroili²², L. Sun⁵⁷, W. Sutcliffe⁵³, K. Swientek²⁷, S. Swientek⁹, V. Syropoulos⁴², M. Szczekowski²⁸, P. Szczypka^{39,38}, T. Szumlak²⁷, S. T'Jampens⁴, M. Teklishyn⁷, G. Tellarini^{16,f}, F. Teubert³⁸, C. Thomas⁵⁵, E. Thomas³⁸, J. van Tilburg⁴¹, V. Tisserand⁴, M. Tobin³⁹, J. Todd⁵⁷, S. Tolk⁴², L. Tomassetti^{16,f}, D. Tonelli³⁸, S. Topp-Joergensen⁵⁵, N. Torr⁵⁵, E. Tournefier⁴, S. Tourneur³⁹, K. Trabelsi³⁹, M.T. Tran³⁹, M. Tresch⁴⁰, A. Trisovic³⁸, A. Tsaregorodtsev⁶, P. Tsopelas⁴¹, N. Tuning⁴¹, M. Ubeda Garcia³⁸, A. Ukleja²⁸, A. Ustyuzhanin⁶⁴, U. Uwer¹¹, C. Vacca^{15,e}, V. Vagnoni¹⁴, G. Valenti¹⁴, A. Vallier⁷, R. Vazquez Gomez¹⁸, P. Vazquez Regueiro³⁷, C. Vázquez Sierra³⁷, S. Vecchi¹⁶, J.J. Velthuis⁴⁶, M. Veltri^{17,h}, G. Veneziano³⁹, M. Vesterinen¹¹, JVV B Viana Barbosa³⁸, B. Viaud⁷, D. Vieira², M. Vieites Diaz³⁷, X. Vilasis-Cardona^{36,p}, A. Vollhardt⁴⁰, D. Volyanskyy¹⁰, D. Voong⁴⁶, A. Vorobyev³⁰, V. Vorobyev³⁴, C. Voß⁶³, J.A. de Vries⁴¹, R. Waldi⁶³, C. Wallace⁴⁸, R. Wallace¹², J. Walsh²³, S. Wandernoth¹¹, J. Wang⁵⁹, D.R. Ward⁴⁷, N.K. Watson⁴⁵, D. Websdale⁵³, M. Whitehead⁴⁸, D. Wiedner¹¹, G. Wilkinson^{55,38}, M. Wilkinson⁵⁹, M.P. Williams⁴⁵, M. Williams⁵⁶, H.W. Wilschut⁶⁶, F.F. Wilson⁴⁹, J. Wimberley⁵⁸, J. Wishahi⁹, W. Wislicki²⁸, M. Witek²⁶, G. Wormser⁷, S.A. Wotton⁴⁷, S. Wright⁴⁷, K. Wyllie³⁸, Y. Xie⁶¹, Z. Xing⁵⁹, Z. Xu³⁹, Z. Yang³, X. Yuan³⁴, O. Yushchenko³⁵, M. Zangoli¹⁴, M. Zavertyaev^{10,b}, L. Zhang³, W.C. Zhang¹², Y. Zhang³, A. Zhelezov¹¹, A. Zhokhov³¹, L. Zhong³.

¹ Centro Brasileiro de Pesquisas Físicas (CBPF), Rio de Janeiro, Brazil

² Universidade Federal do Rio de Janeiro (UFRJ), Rio de Janeiro, Brazil

³ Center for High Energy Physics, Tsinghua University, Beijing, China

⁴ LAPP, Université de Savoie, CNRS/IN2P3, Annecy-Le-Vieux, France

⁵ Clermont Université, Université Blaise Pascal, CNRS/IN2P3, LPC, Clermont-Ferrand, France

⁶ CPPM, Aix-Marseille Université, CNRS/IN2P3, Marseille, France

⁷ LAL, Université Paris-Sud, CNRS/IN2P3, Orsay, France

⁸ LPNHE, Université Pierre et Marie Curie, Université Paris Diderot, CNRS/IN2P3, Paris, France

⁹ Fakultät Physik, Technische Universität Dortmund, Dortmund, Germany

¹⁰ Max-Planck-Institut für Kernphysik (MPIK), Heidelberg, Germany

¹¹ Physikalisches Institut, Ruprecht-Karls-Universität Heidelberg, Heidelberg, Germany

¹² School of Physics, University College Dublin, Dublin, Ireland

¹³ Sezione INFN di Bari, Bari, Italy

¹⁴ Sezione INFN di Bologna, Bologna, Italy

¹⁵ Sezione INFN di Cagliari, Cagliari, Italy

¹⁶ Sezione INFN di Ferrara, Ferrara, Italy

¹⁷ Sezione INFN di Firenze, Firenze, Italy

¹⁸ Laboratori Nazionali dell'INFN di Frascati, Frascati, Italy

¹⁹ Sezione INFN di Genova, Genova, Italy

²⁰ Sezione INFN di Milano Bicocca, Milano, Italy

²¹ Sezione INFN di Milano, Milano, Italy

²² Sezione INFN di Padova, Padova, Italy

²³ Sezione INFN di Pisa, Pisa, Italy

²⁴ Sezione INFN di Roma Tor Vergata, Roma, Italy

²⁵ Sezione INFN di Roma La Sapienza, Roma, Italy

²⁶ Henryk Niewodniczanski Institute of Nuclear Physics Polish Academy of Sciences, Kraków, Poland

²⁷ AGH - University of Science and Technology, Faculty of Physics and Applied Computer Science, Kraków, Poland

²⁸ National Center for Nuclear Research (NCBJ), Warsaw, Poland

²⁹ Horia Hulubei National Institute of Physics and Nuclear Engineering, Bucharest-Magurele, Romania

- 30 Petersburg Nuclear Physics Institute (PNPI), Gatchina, Russia
31 Institute of Theoretical and Experimental Physics (ITEP), Moscow, Russia
32 Institute of Nuclear Physics, Moscow State University (SINP MSU), Moscow, Russia
33 Institute for Nuclear Research of the Russian Academy of Sciences (INR RAN), Moscow, Russia
34 Budker Institute of Nuclear Physics (SB RAS) and Novosibirsk State University, Novosibirsk, Russia
35 Institute for High Energy Physics (IHEP), Protvino, Russia
36 Universitat de Barcelona, Barcelona, Spain
37 Universidad de Santiago de Compostela, Santiago de Compostela, Spain
38 European Organization for Nuclear Research (CERN), Geneva, Switzerland
39 Ecole Polytechnique Fédérale de Lausanne (EPFL), Lausanne, Switzerland
40 Physik-Institut, Universität Zürich, Zürich, Switzerland
41 Nikhef National Institute for Subatomic Physics, Amsterdam, The Netherlands
42 Nikhef National Institute for Subatomic Physics and VU University Amsterdam, Amsterdam, The Netherlands
43 NSC Kharkiv Institute of Physics and Technology (NSC KIPT), Kharkiv, Ukraine
44 Institute for Nuclear Research of the National Academy of Sciences (KINR), Kyiv, Ukraine
45 University of Birmingham, Birmingham, United Kingdom
46 H.H. Wills Physics Laboratory, University of Bristol, Bristol, United Kingdom
47 Cavendish Laboratory, University of Cambridge, Cambridge, United Kingdom
48 Department of Physics, University of Warwick, Coventry, United Kingdom
49 STFC Rutherford Appleton Laboratory, Didcot, United Kingdom
50 School of Physics and Astronomy, University of Edinburgh, Edinburgh, United Kingdom
51 School of Physics and Astronomy, University of Glasgow, Glasgow, United Kingdom
52 Oliver Lodge Laboratory, University of Liverpool, Liverpool, United Kingdom
53 Imperial College London, London, United Kingdom
54 School of Physics and Astronomy, University of Manchester, Manchester, United Kingdom
55 Department of Physics, University of Oxford, Oxford, United Kingdom
56 Massachusetts Institute of Technology, Cambridge, MA, United States
57 University of Cincinnati, Cincinnati, OH, United States
58 University of Maryland, College Park, MD, United States
59 Syracuse University, Syracuse, NY, United States
60 Pontifícia Universidade Católica do Rio de Janeiro (PUC-Rio), Rio de Janeiro, Brazil, associated to²
61 Institute of Particle Physics, Central China Normal University, Wuhan, Hubei, China, associated to³
62 Departamento de Física , Universidad Nacional de Colombia, Bogota, Colombia, associated to⁸
63 Institut für Physik, Universität Rostock, Rostock, Germany, associated to¹¹
64 National Research Centre Kurchatov Institute, Moscow, Russia, associated to³¹
65 Instituto de Física Corpuscular (IFIC), Universitat de Valencia-CSIC, Valencia, Spain, associated to³⁶
66 Van Swinderen Institute, University of Groningen, Groningen, The Netherlands, associated to⁴¹
67 Celal Bayar University, Manisa, Turkey, associated to³⁸

^a Universidade Federal do Triângulo Mineiro (UFTM), Uberaba-MG, Brazil

^b P.N. Lebedev Physical Institute, Russian Academy of Science (LPI RAS), Moscow, Russia

^c Università di Bari, Bari, Italy

^d Università di Bologna, Bologna, Italy

^e Università di Cagliari, Cagliari, Italy

^f Università di Ferrara, Ferrara, Italy

^g Università di Firenze, Firenze, Italy

^h Università di Urbino, Urbino, Italy

ⁱ Università di Modena e Reggio Emilia, Modena, Italy

^j Università di Genova, Genova, Italy

^k Università di Milano Bicocca, Milano, Italy

^l Università di Roma Tor Vergata, Roma, Italy

- ^m *Università di Roma La Sapienza, Roma, Italy*
- ⁿ *Università della Basilicata, Potenza, Italy*
- ^o *AGH - University of Science and Technology, Faculty of Computer Science, Electronics and Telecommunications, Kraków, Poland*
- ^p *LIFAELS, La Salle, Universitat Ramon Llull, Barcelona, Spain*
- ^q *Hanoi University of Science, Hanoi, Viet Nam*
- ^r *Università di Padova, Padova, Italy*
- ^s *Università di Pisa, Pisa, Italy*
- ^t *Scuola Normale Superiore, Pisa, Italy*
- ^u *Università degli Studi di Milano, Milano, Italy*
- ^v *Politecnico di Milano, Milano, Italy*